Available online at www.sciencedirect.com
SCIENCE DIRECT®
Journal of Organometallic Chemistry 684 (2003) 338–350
Journal of Organometallic Chemistry
www.elsevier.com/locate/jorganchem

$Cl_4(PhCN)W(NPh)$ as a single-source MOCVD precursor for deposition of tungsten nitride (WN_x) thin films

Omar J. Bchir [a], Kelly M. Green [a], Mark S. Hlad [a], Timothy J. Anderson [a,*], Benjamin C. Brooks [b], Corey B. Wilder [b], David H. Powell [b], Lisa McElwee-White [b,*]

[a] Department of Chemical Engineering, University of Florida, Gainesville, FL 32611-6005, USA
[b] Department of Chemistry, University of Florida, Gainesville, FL 32611-7200, USA

Received 10 March 2003; received in revised form 3 June 2003; accepted 3 June 2003

Dedicated to Professor E.O. Fischer on the occasion of his 85th birthday

Abstract

The tungsten phenylimido complex $Cl_4(PhCN)W(NPh)$ (**2b**) was tested as a single-source precursor for growth of tungsten nitride (WN_x) thin films, and results were compared to films previously deposited from the isopropylimido complexes $Cl_4(RCN)W(N^iPr)$ (**1a**, R = CH_3; **1b**, R = Ph). Films deposited from **2b** exhibited growth rates ranging from 2 to 21 Å min^{-1} over a temperature range of 475–750 °C, and the apparent activation energy for film growth in the kinetically controlled regime was 1.41 ± 0.58 eV. Amorphous β-WN_x films were deposited below 500 °C, with minimum film resistivity and sheet resistance of 225 μΩ-cm and 75 Ω/□, respectively, observed for deposition at 475 °C. In contrast, films deposited from the isopropylimido complexes **1a**,**b** exhibited higher growth rates and higher nitrogen content over a similar temperature range. These differences are attributed to the higher dissociation energy of the imido N–C bond in phenylimido complex **2b**. Mass spectrometry fragmentation patterns are consistent with this behavior.

Keywords: Tungsten; Imido; Nitride; Chemical vapor deposition; Diffusion barrier

1. Introduction

As feature sizes on integrated circuits (ICs) become smaller, the need for a thin, effective barrier to prevent intermixing of silicon and metallization layers becomes more critical. Copper is being increasingly used as the interconnect metallization for various levels on ICs due to its lower bulk resistivity, greater resistance to electromigration, and diminished contact resistance relative to aluminum [1]. Unfortunately, copper has much higher mass diffusivity in silicon than does aluminum, making diffusion barrier performance even more crucial [2]. Ideally, diffusion barrier materials used in ICs should have amorphous film structure, low resistivity, good conformality over different device features, and low deposition temperature (≤ 450 °C).

Material selection is vital to a successful diffusion barrier. Use of refractory metal thin films as diffusion barriers failed due to the formation of grain boundaries, which are facile pathways for Cu mFigration to the underlying substrate [3]. Refractory metal nitrides, such as tantalum nitride (TaN) and tungsten nitride (WN_x), however, are promising diffusion barrier materials for Cu metallization [4]. Excess nitrogen in these films accumulates at the grain boundaries during polycrystal formation and is believed to hinder Cu diffusion. Nitrogen atoms at the grain boundary significantly reduce diffusion through a "stuffing" process, which involves repulsive Cu–N interactions [5,6]. Although TaN is currently used as a copper diffusion barrier material for intermediate level wiring in IC applications [7], WN_x offers several advantages. These include

* Corresponding authors. Tel.: +1-352-392-8768; fax: +1-352-846-0296 (L.M.-W.); tel.: +1-352-392-0946; fax: +1-352-392-9513 (T.J.A.).
E-mail addresses: tim@nersp.nerdc.ufl.edu (T.J. Anderson), lmwhite@chem.ufl.edu (L. McElwee-White).

0022-328X/03/$ - see front matter © 2003 Elsevier B.V. All rights reserved.
doi:10.1016/S0022-328X(03)00769-1

superior adhesion to copper [8], more efficient subsequent processing (e.g. ease in use of chemical mechanical polishing or CMP) [9], and potential use as an electrode layer to enable seedless copper electrodeposition [10].

In addition to material selection, diffusion barrier properties are heavily influenced by the choice of technique and conditions used to deposit the film. Chemical vapor deposition (CVD) operating in the kinetically limited growth regime is a technique that is well suited to deposit highly conformal films. Selection of appropriate precursors for the CVD process may enable deposition of amorphous films at low temperature. One variant of CVD depends on reduction of halide precursors to deposit films. In another variant, metal-organic chemical vapor deposition (MOCVD), material is deposited on the substrate surface by reaction of one or more carbon-containing vapor phase precursor compounds. Both of these variants are often operated at low pressure to increase mass transfer rates to the extent that deposition is reaction limited, thus producing more conformal films.

The typical strategies for CVD of multi-element barrier materials involve the use of either single-source or co-reactant precursors. Co-reactant deposition uses a separate precursor for each element desired in the film; hence, bonds between these elements must be formed by intermolecular processes during deposition. In contrast, a single-source precursor already has bonds established between the elements that will comprise the film prior to deposition. This approach is particularly useful when the bond strengths in the individual precursor candidates, and thus decomposition temperatures, are quite different.

Previous examples of WN_x deposited by CVD are dominated by co-reactant systems using NH_3 as the nitrogen source (Scheme 1). Early examples employed WF_6, WCl_6 or WO_3 as the tungsten source [11–18].

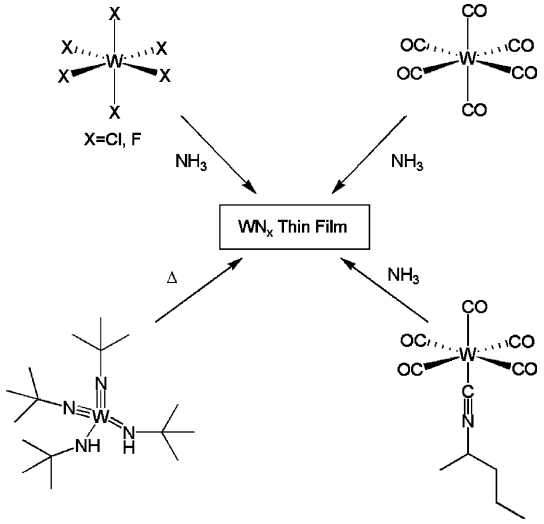

Scheme 1.

Unfortunately, the high temperatures required for reaction of metal halides with NH_3 (greater than 500 °C) [19], along with the resulting reactive by-products (e.g. hydrogen halides) [20,21], are two major drawbacks to barrier deposition by co-reactant metal halide processes.

More recently, organometallic precursors have been employed in co-reactant systems. Accordingly, $W(CO)_6$ and NH_3 have been used to deposit amorphous WN_x films below 275 °C [22]. In a similar study, deposition of WN_x from $W(CO)_5(C_5H_{11}NC)$ and NH_3 was reported in the temperature range 250–400 °C [23]. In the sole prior example of a single-source precursor for WN_x deposition, polycrystalline thin films were obtained by pyrolyzing the bis(imido) bis(amido) complex $(^tBuNH)_2W(N^tBu)_2$ in the temperature range 450–650 °C [24–26].

Recently, we reported MOCVD of amorphous WN_x thin films from benzonitrile solutions of the single-source imido precursor $Cl_4(CH_3CN)W(N^iPr)$ (**1a**) as a mixture with its benzonitrile derivative **1b** [27,28]. The properties of these films were compared with those of films deposited from the other reported tungsten imido precursor, $(^tBuNH)_2W(N^tBu)_2$ [27,28]. Imido complexes are attractive candidates for MOCVD of tungsten nitride since the strong W≡N multiple bond is likely to survive as other moieties dissociate during film deposition. Furthermore, the simple synthesis of **1a**,**b** can easily be adapted to produce a series of related complexes containing different alkyl or aryl substituents on the imido ligand. This feature allows variation of the N–C bond dissociation energy, which is important since this bond must be cleaved during the CVD process. The N–C (imido nitrogen to 2° alkyl) bond of **1a**,**b** will be relatively weak, compared to the N–aryl bond of the phenylimido complex $Cl_4(PhCN)W(NPh)$ (**2b**). We now report the growth of WN_x films from **2b**, and discuss the film deposition and the properties of the resulting material. Comparison of material deposited from **1a**,**b** and **2b** provides insight into the effect of the imido N–C bond strength on the MOCVD process.

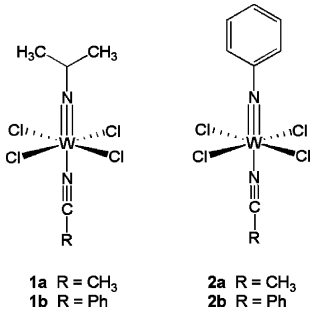

2. Experimental

2.1. General (precursor synthesis)

The complex $Cl_4(OEt_2)W(NPh)$ (**3**) was synthesized as previously described by Schrock et al. [29]. The benzonitrile complex $Cl_4(PhCN)W(NPh)$ (**2b**) was not isolated, but was produced in situ by the substitution of the ether ligand of **3** with benzonitrile following solvation in the 10:1 $PhCN–Et_2O$ co-solvent utilized for the deposition experiments (vide infra). The acetonitrile complex $Cl_4(CH_3CN)W(NPh)$ (**2a**) was prepared as previously reported by Nielson [30].

2.2. Mass spectrometry

All mass spectral analyses were performed using a Finnigan MAT95Q hybrid sector mass spectrometer (Thermo Finnigan, San Jose, CA). Electron ionization (EI) was carried out in positive ion mode using electrons of 70 eV potential and a source temperature of 200 °C. Negative ion electron capture chemical ionization (NCI) used methane as the bath gas at an indicate pressure of 2×10^{-5} Torr, an electron energy of 100 V and a source temperature of 120 °C. All samples were introduced via a controlled temperature probe with heating and cooling enabling temperature control down to 35 °C. The mass resolving power ($m/\Delta m$) was 5000 full width-half maximum (FWHM).

2.3. Film growth studies

The solid precursor was dissolved in 10:1 benzonitrile:ether at a concentration of 7.5 mg ml^{-1}, loaded into a syringe and pumped into a nebulizer. Operation of the nebulizer was described previously [28]. Experiments were conducted in a custom-built vertical quartz cold wall CVD reactor system. P-type boron doped Si (100) substrates with resistivity of 1–2 Ω-cm were used for the film growths. Growths were conducted for a fixed time of 150 min at temperatures ranging from 450 to 800 °C. The system was maintained at vacuum by a mechanical roughing pump, with the operating pressure fixed at 350 Torr. Hydrogen (H_2) carrier gas was used for the depositions.

Film structure was examined by X-ray diffraction (XRD) on a Philips APD 3720, operating from 5 to 85 2θ degrees with $Cu–K_\alpha$ radiation. Film composition was determined by Auger electron spectroscopy (AES) using a Perkin–Elmer PHI 660 Scanning Auger Multiprobe, while XPS data were collected with a Perkin–Elmer PHI 5100 ESCA System using an Mg anode X-ray source. Film resistivity was measured with an Alessi Industries four-point probe. Film thickness was estimated by cross-sectional scanning electron microscopy (X-SEM) on a JEOL JSM-6400, with growth rate calculated by dividing film thickness by deposition time.

3. Results and discussion

3.1. Mass spectrometry

As noted before, care must be taken in using mass spectral data to predict CVD behavior since the latter is thermal in nature [31]. Nevertheless, mass spectrometry does provide insights into the relative fragmentation characteristics of various precursors [32]. In order to provide a direct comparison of mass spectral data for a phenylimido complex and its isopropyl analogue, the acetonitrile adduct $Cl_4(CH_3CN)W(NPh)$ (**2a**) was prepared as a model for **2b**. Precedent for the modeling of **2a** by **2b** is provided by the virtually identical ion fragmentation patterns for the isopropyl imido complexes **1a** and **1b** [28]. Mass spectrometry results for **2a** could then be compared to our previously reported data for the isopropyl imido complex $Cl_4(CH_3CN)W(N^iPr)$ (**1a**) [28]. Accordingly, **2a** was analyzed using both positive ion electron-impact (EI) and NCI methods.

The EI and NCI mass spectra of **2a** are depicted in Fig. 1, and the relative abundances of the observed peaks of the phenylimido and isopropylimido complexes **2a** and **1a** are summarized in Table 1. As observed in the mass spectra of the isopropyl precursor, no molecular ion was detected for **2a** using either ionization method. The base peak in the EI spectrum occurs at m/z 382, and corresponds to the fragment $[Cl_3W(NPh)]^+$. The highest mass peak observed in the EI spectrum was $[Cl_4W(NPh)]^+$ at m/z 417 (9% abundance). Interestingly, although the high mass envelopes correspond to fragments in which acetonitrile is lost, only a small amount ($\sim$1% abundance) of the $[CH_3CN]^+$ ion was detected at m/z 41 in the EI spectrum of **2a**. The presence of the $[Cl_4W]^+$ and $[Cl_3W]^+$ fragments suggests cleavage of the W–N bond occurs in the gas phase. Furthermore, observation of the $[Ph]^+$ fragment (m/z 77) indicates that the critical N–Ph bond is broken to some extent under EI conditions; however, there is no evidence of a metal nitrido fragment in the resulting spectrum. Moreover, the base peak in the NCI spectrum corresponds to $[Cl_4W(NPh)]^-$ (m/z 417) while the mass envelope of the nitride fragment $[Cl_4WN]^-$ (m/z 340) has a relative abundance of 4%. The presence of the fragment $[Cl_5W(NPh)]^-$ suggests that the nitrile ligand of **2a** is removed during the process of heating the condensed phase sample to afford $[W(NPh)Cl_4]_2$ prior to ionization.

The mass spectral data for phenylimido complex **2a** and isopropylimido complex **1a** show some similarities. For both, the most prevalent ion on the high mass end of the EI spectrum corresponds to $[Cl_3W(NR)]^+$,

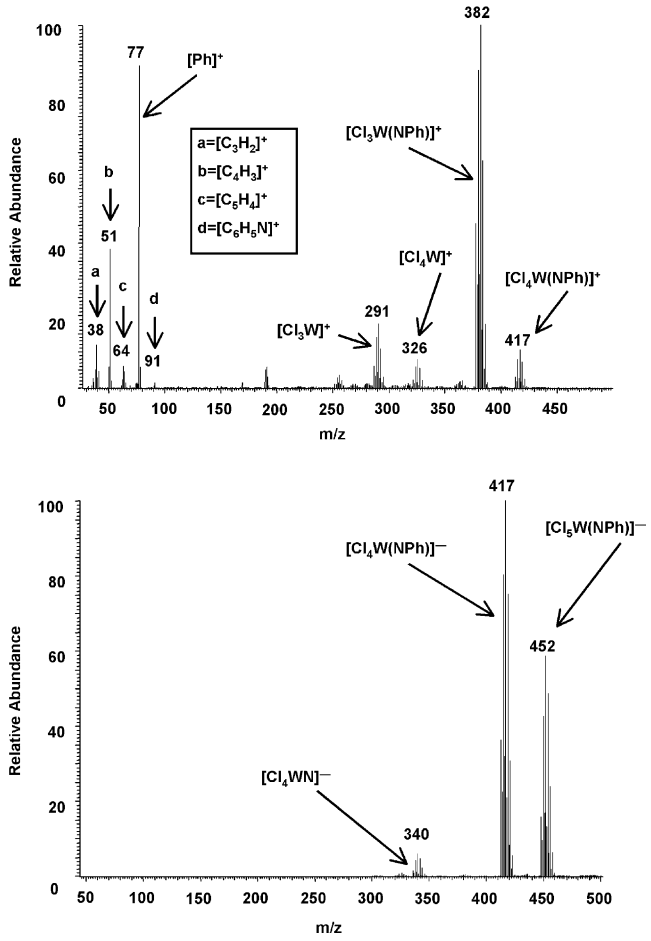

Fig. 1. Positive ion electron-impact ionization (EI) and negative ion electron capture chemical ionization (CI) mass spectra of **2a**.

although **2a** does also exhibit lower abundance peaks from $[Cl_4W(NPh)]^+$. This, coupled with the lack of molecular ion signals, is consistent with high lability of the nitrile ligand in both complexes. Moreover, the presence of the $[Cl_5W(NPh)]^-$ fragment in the NCI spectrum suggests that the lability of the nitrile ligand results in partial conversion of **2a** to the dimer $[W(NPh)Cl_4]_2$ prior to ionization. The observation of this chloride transfer process in **2a**, but not **1a**, is consistent with the greater electron withdrawing nature of the phenyl substituent, as compared to isopropyl.

The most notable difference in the spectra of **2a** and **1a** concerns the fragments $[Cl_3WNH]^+$ and $[Cl_4WN]^-$. Since these ions are derived from cleavage of the N–R bond of the imido moiety, they are critical to the CVD process. As shown in Table 1, $[Cl_3WNH]^+$ appears in the EI spectrum of **1a** with a relative abundance of 78%; however, this fragment is not present in the spectrum of the phenylimido complex **2a**. Nevertheless, the presence of $[Ph]^+$ indicates the N–Ph bond is broken to a certain extent under EI conditions. The ion $[PhN]^+$ (*m*/*z* 91) was observed in very small relative abundance ($<1\%$), and its subsequent fragmentation may be responsible for

Table 1
Summary of relative abundances for positive ion EI and negative ion NCI mass spectra of tungsten imido complexes $Cl_4(CH_3CN)W(NPh)$ (**2a**) and $Cl_4(CH_3CN)W(N^iPr)$ (**1a**)

Complex	EI fragments	NCI fragments	*m*/*z*	Abundance [a,b]
$Cl_4(CH_3CN)W(NPh)$ (**2a**)	$[Cl_4W(NPh)]^+$		417	9
	$[Cl_3W(NPh)]^+$		382	100
	$[Cl_4W]^+$		326	7
	$[Cl_3W]^+$		291	15
	$[PhN]^+$		91	<1
	$[Ph]^+$		77	22
	$[C_5H_4]^+$		64	1
	$[C_4H_3]^+$		51	10
	$[CH_3CN]^+$		41	1
	$[C_3H_2]^+$		38	1
		$[Cl_5W(NPh)]^-$	452	23
		$[Cl_4W(NPh)]^-$	417	100
		$[Cl_4WN]^-$	340	4
$Cl_4(CH_3CN)W(N^iPr)$ (**1a**)	$[Cl_3W(N^iPr)]^+$		348	100
	$[Cl_4W]^+$		326	26
	$[Cl_3WNH]^+$		306	78
	$[Cl_3W]^+$		291	30
	$[CH_3CN]^+$		41	24
		$[Cl_4W(N^iPr)]^-$	383	42
		$[Cl_4WN]^-$	340	100

[a] Relative abundances were adjusted by summing the observed intensities for the predicted peaks of each mass envelope and normalizing the largest sum to 100%.
[b] Values for **1a** are from Ref. [28].

the small clusters of peaks centered at *m*/*z* 64, 51 and 38 [33]. Even more striking is the fact that the $[Cl_4WN]^-$ fragment is the base peak in the NCI spectrum of **1a**, but only accounts for 4% relative abundance in the phenylimido complex **2a**.

In relation to the use of $Cl_4(PhCN)W(NPh)$ (**2b**) as a precursor for tungsten nitride deposition, the mass spectral data of **2a** and **1a** suggest that the N–Ph bond is more difficult to break than the N–^{i}Pr bond. This is consistent with the homolytic bond strength of the two N–R moieties [34]. If N–Ph bond cleavage were involved in the rate determining step, **2b** would be expected to require higher deposition temperatures relative to the isopropyl system. The stronger N–Ph bond may also affect growth rate and composition of the deposited films. Additionally, these data suggest that replacing the phenyl moiety with a group that will cleave more readily (e.g. allyl) could decrease the deposition temperature and improve the compositional characteristics of the WN_x films.

3.2. Volatilization of the precursor

Deposition of thin films by MOCVD requires transport of the solid phenylimido precursor **2b** to the reactor in the vapor phase. Previous tests with similar complexes in a solid source delivery system resulted in minimal

precursor transport, due to the low vapor pressure of the compounds. Transport difficulties were overcome by using a nebulizer to generate an aerosol of the precursor/solvent mixture, which is conveyed by carrier gas to the reactor. Although benzonitrile is an appropriate solvent for deposition from isopropylimido complexes **1a**,**b**, poor solubility of the phenylimido complexes in benzonitrile necessitated a co-solvent mixture of 10:1 benzonitrile:ether to achieve the same precursor concentration previously used with **1a**,**b**. To determine the impact, if any, of the co-solvent on film composition, acetonitrile was tested in place of ether. AES results indicated similar film compositions regardless of the co-solvent used.

3.3. Film structure

The films typically had a smooth, shiny metallic appearance with color varying from black to gold, depending on the deposition conditions. The desired WN_x film structure and stoichiometry is face centered cubic (FCC) β-W_2N (β-WN_x, $x = 0.5$), since this phase has the lowest resistivity. The XRD spectrum in Fig. 2a is consistent with amorphous film deposition from **2b** at 475 °C, as evidenced by a flat profile with no characteristic β-WN_x peaks. In contrast, the XRD spectrum shown in Fig. 2b indicates polycrystalline film deposition at 750 °C. Four characteristic peaks are evident, with relative peak intensities indicating that no preferred crystal orientation exists. Although the relative peak intensities in Fig. 2b are consistent with the pattern for polycrystalline β-W_2N, the 2θ peak positions lie between the standard values for β-W_2N and β-W_2C, which are shown in Fig. 2c.

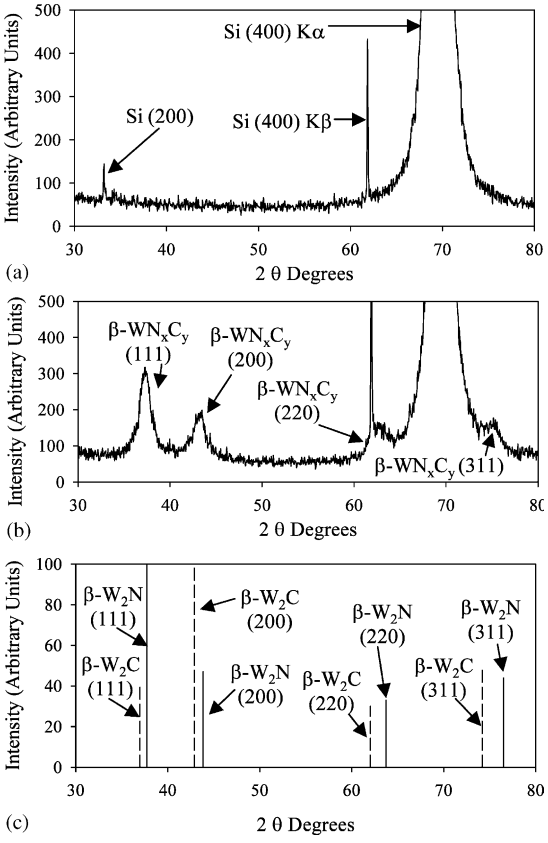

Fig. 2. XRD spectra of WN_xC_y grown from **2b** on Si (100) in a H_2 atmosphere at (a) 475 °C and (b) 750 °C; (c) shows standard powder diffraction plots for β-W_2N (solid lines) and β-W_2C (dashed lines).

Peak positions between these standard values suggest that carbon is mixing with nitrogen and vacancies on tungsten's interstitial sublattice to form β-WN_xC_y polycrystals. For the spectrum in Fig. 2b, primary reflections at 37.13 and 43.08 2θ degrees are consistent with (111) and (200) β-WN_xC_y growth planes, while additional reflections at 62.73 and 74.98 2θ degrees indicate (220) and (311) planes, respectively. No peaks arising from the hexagonal WN or WC phases, or the body centered cubic (BCC) α-W phase were evident for any of the films.

Fig. 3 illustrates the evolution of film crystallinity with deposition temperature for growth from **2b**. The trend of increasing crystallinity with deposition temperature is similar to that observed for the isopropyl imido precursor **1b** [28]. At the lowest deposition temperature (475 °C), the characteristic β-WN_x peaks are not observed, indicating that the film is amorphous.

As the temperature increases to 500 °C, peaks appear at 23.48 (not shown) and 47.98 2θ degrees, consistent with formation of tungsten oxide (WO_x, $x \approx 3$). Repeated attempts to deposit films at 500 °C resulted in formation of tungsten oxide, while peaks consistent with WN_x are seen at all deposition temperatures above this. Reproducible deposition of tungsten oxide at a single temperature suggests that an air leak in the reactor system is unlikely to be the source of oxygen. Microstructure dependent, post-growth oxygen incorporation is a likely cause of oxide formation, especially for low temperature, "clean" tungsten films with low carbon

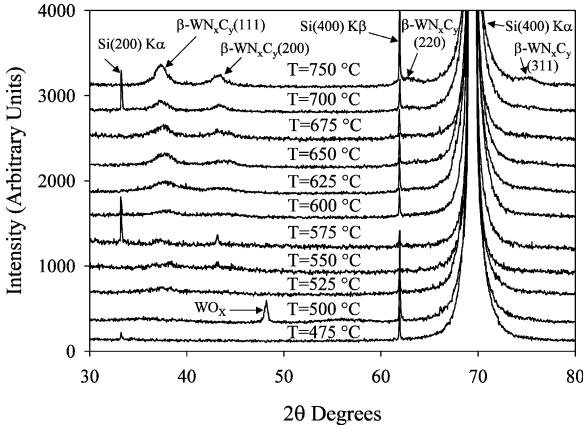

Fig. 3. Change in XRD pattern with deposition temperature for WN_xC_y grown from **2b** on Si (100) in a H_2 atmosphere.

and nitrogen levels. This is due to lower contamination levels, which make these films less resistant to oxygen in-diffusion and reaction. The existence of a second oxygen incorporation pathway involving the Et_2O co-solvent, however, cannot be ruled out. Diethyl ether is known to undergo both homogeneous and heterogeneous decomposition at temperatures near 500 °C [35,36]. Although oxide formation still occurs for films grown at 500 °C from Cl_4(PhCN)W(NPh) (**2b**) in a benzonitrile/acetonitrile mixture (no Et_2O present), the size of the oxide crystallites is larger when the ether complex Cl_4-(Et_2O)W(NPh) (**3**) was used to generate precursor or when Et_2O is the co-solvent. Even though the film is amorphous at 475 °C, indicating that inadequate thermal energy is available to produce oxide polycrystals, the possibility of oxygen incorporation similar to that at 500 °C cannot be ruled out. High levels of oxygen in the amorphous film, as demonstrated by AES data (vide infra), support this possibility.

A broad peak near 38.03 2θ degrees, which is above the standard peak position for β-W_2N (111), appears for deposition at 525 °C, and indicates the presence of nitrogen-deficient polycrystalline β-WN_x (111). A broad peak at 44.03 2θ degrees for deposition at 550 °C indicates the first appearance of β-WN_x (200). As the temperature increases to 600 °C, film peak positions shift below the standard β-W_2N positions, indicating that β-WN_xC_y deposition is occurring. Broad peaks emerge at 62.93 and 75.58 2θ degrees for deposition at 700 °C, indicating β-WN_xC_y (220) and (311) growth. The peaks sharpen further as the temperature increases to 750 °C, due to polycrystalline grain growth. Peak sharpness decreased somewhat for the film deposited at 800 °C (not shown), which is likely due to a decrease in film thickness as measured by XSEM (vide infra). Decreased film thickness may be caused by rapid desorption of reactants from the film surface due to high temperatures or by gas phase reactions, which deplete the amount of reactant available at the film surface. Some films deposited between 475 and 600 °C displayed additional peaks at 32.98 and/or 61.68 2θ degrees, representing reflections from the underlying Si consistent with Si (200) Kα and Si (400) Kβ radiation, respectively.

At the highest deposition temperature, minimal nitrogen and high carbon levels suggest that the stoichiometry of the β-WN_xC_y polycrystals may be approaching β-WC_y deposition. A shift in the position of the peaks toward β-W_2C at higher deposition temperature provides evidence of this trend.

3.4. Film composition

AES results for films deposited from the phenylimido complex **2b** indicate the presence of W, N, C and O (Fig. 4). No chlorine was detected in the films by AES or XPS, placing an upper limit of ~1 at.% on Cl content. HCl is the thermodynamically favored gas phase chlorine-containing species, and was observed by residual gas analysis during deposition from **1a**,**b**. It is assumed that HCl is the dominant gas phase chlorine-containing species for deposition from **2b** as well. Neither Cl_2 nor chlorinated hydrocarbons were detected in the reactor effluent, leading to the conclusion that chlorine is lost from the precursor as HCl. From 475 to 500 °C, the carbon level is constant at approximately 3–5 at.%. The carbon content jumps from 5 to 14 at.% between 500 and 525 °C. Although XRD indicates β-WN_x polycrystalline deposition at 525 °C, results for growth rate and sheet resistance (vide infra) at this temperature show strong deviation from the trends evident between 550 and 750 °C. Given the proximity in deposition temperature of the carbon spike (525 °C) to the anomalous tungsten oxide formation seen in the XRD (500 °C), the two phenomena may be related. Above 550 °C, the carbon content rises steadily from 9 to 22 at.% at 750 °C. The increase in carbon content from lowest to highest deposition temperature reflects the increasing tendency of the hydrocarbon groups present in the precursor ligands and the solvent to deposit in the films at higher growth temperature.

The initial nitrogen content of films grown at 475 °C was 1 at.%. The nitrogen content increased to a maximum value of 3 at.% at 525 °C as a consequence of decreased oxygen concentration through this range. The nitrogen concentration then decreased with increasing temperature, dropping below 1 at.% above 700 °C. Although metal nitride barriers typically exhibit low nitrogen content at higher deposition temperatures (due to desorption of N_2 gas), the films deposited from **2b** were nitrogen-deficient throughout the temperature range studied. This nitrogen deficiency in the films contrasts with XRD results in Fig. 3, which indicate β-WN_x polycrystal growth at lower temperatures. This may indicate that β-WN_xC_y polycrystal formation begins at temperatures below 600 °C, with carbon filling the excess vacancies present in the polycrystals due to nitrogen deficiency.

Although the value of y in β-WN_xC_y should be relatively small at the lower deposition temperatures, it may be sufficiently large to shift the XRD peak position to lower values of 2θ (and concomitantly increase the lattice parameter, vide infra), even at the lower temperatures. It should also be noted that preferential incorporation of carbon and removal of nitrogen by Ar^+ sputtering during AES analysis has been reported to cause artificially high carbon and low nitrogen concentration readings [37]. Since the AES data were collected after 2.0 min of sputter, artificially high carbon and low nitrogen compositions may have been observed. In addition, the lack of a standard film sample for calibration of elemental concentrations means that AES

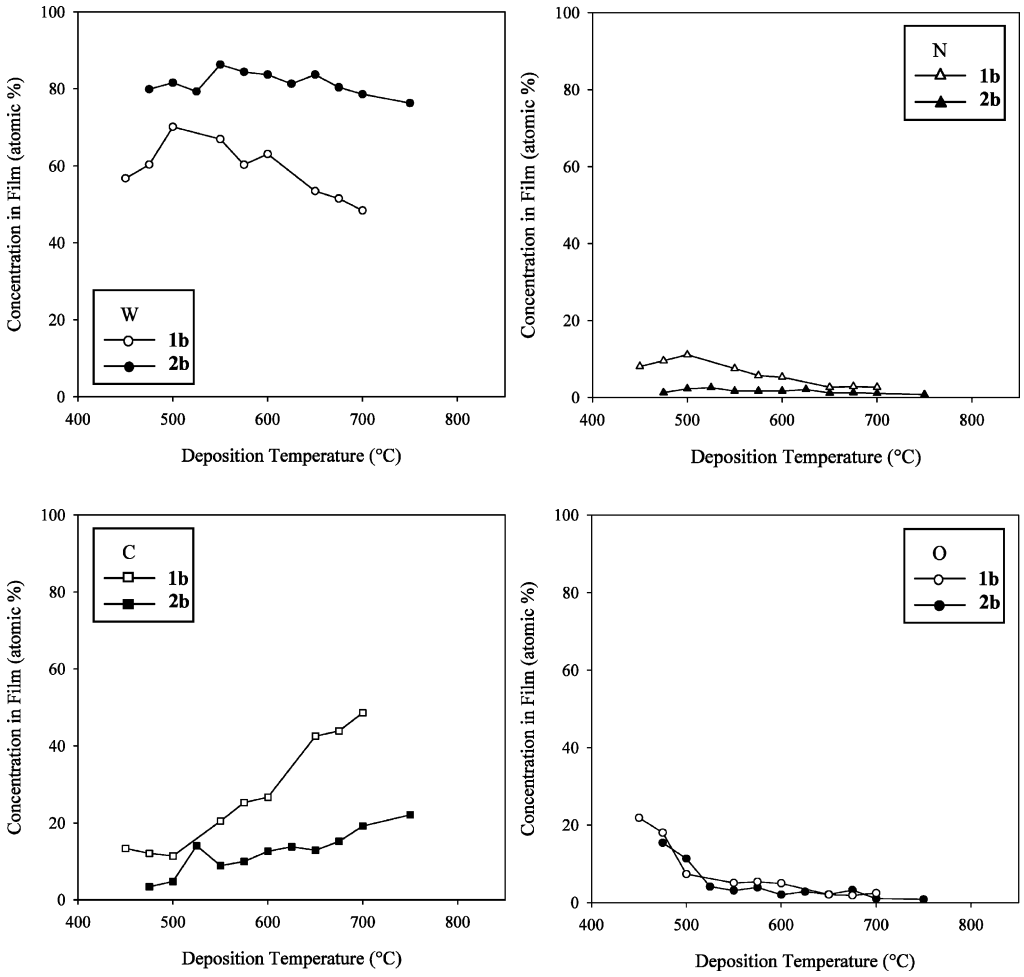

Fig. 4. Comparison of tungsten, nitrogen, carbon and oxygen content in the WN_xC_y films grown from the **1b** and **2b** compounds. Data are from AES measurements after 2.0 min sputter.

data may vary up to several atom percent from the actual values. Despite the error bars on the concentrations, the AES data serve to identify trends in film composition with deposition temperature.

The slight oxygen contamination in the film samples deposited at higher temperatures likely resulted from post-growth exposure of the film samples to air. The higher oxygen levels in films deposited at and below 500 °C may be influenced by the presence of the Et_2O co-solvent during growth and exposure of the films to air after growth. Incremental AES sputtering showed a steady decrease in oxygen levels with increasing depth into the WN_x films. The oxygen concentration was highest at 475 °C, reaching 15 at.%, and then decreased slightly to 11 at.% at 500 °C. This behavior is consistent with low density and high porosity in the amorphous films deposited below 525 °C, which allow substantial amounts of oxygen to penetrate into the film lattice. High oxygen concentrations ($\sim 20\%$) attributed to air exposure have been reported for porous TiN, TiC and TiCN barriers [38–40]. XPS results for oxygen in the films are consistent with WO_3, which has considerably higher thermodynamic stability than β-WN_x or β-WC_x. For example, values of the Gibbs energy of formation (ΔG_f°) at 750 °C for the WO_3, β-$WN_{0.5}$ and β-$WC_{0.5}$ phases are -579 kJ mol^{-1}, $+21$ kJ mol^{-1}, and -8.5 kJ mol^{-1}, respectively [41–43]. The experimental observation of lower levels of oxygen at higher deposition temperatures is consistent with post-growth oxygen contamination. As the deposition temperature rises from 500 to 525 °C, the oxygen content drops sharply to 4 at.%. This behavior is consistent with the change in crystallinity observed by XRD. As the film crystallizes, it becomes more dense [44], thereby inhibiting post-growth oxygen diffusion into the lattice and decreasing the density of adsorption sites. As deposition temperature increases above 525 °C, the oxygen concentration drops further, falling below 1 at.% above 700 °C. This drop in oxygen levels likely results from film densification (by polycrystal grain growth) and increased carbon levels at higher deposition temperature stuffing the grain boundaries. Porosity of amorphous films grown below

525 °C may be problematic for diffusion barrier applications, since defects in the film may degrade the barrier's resistance to Cu diffusion. A previous report, however, indicates that diffusion barrier performance depends more strongly on film microstructure than film density [45]. In addition, impurities such as O, N and C have been reported to enhance the stability of diffusion barrier films [46].

3.5. Lattice parameter

The dependence of lattice parameter on deposition temperature was determined by XRD using the 2θ position of the (111) β-WN_xC_y diffraction peak, with peak position calibrated to the Si (400) diffraction peak (Fig. 5). The standard β-W_2N (111) and β-W_2C (111) peak positions are 37.735 and 36.977 2θ degrees (Fig. 2c), respectively, and correspond to standard lattice parameter values of 4.126 and 4.236 Å. The position of the (111) reflection peak can vary as a result of a change in composition or a change in the film's residual stress.

Assuming that compositional variation is responsible for the peak shift and, thus, lattice parameter change, trends in the relative concentrations of nitrogen, carbon, and vacancies on the interstitial sublattice can be suggested by coupling the peak shift with the compositions measured by AES (Fig. 4). If the (111) peak position is higher than 37.735 2θ degrees, corresponding to a lattice parameter below 4.126 Å, then minimal carbon, a deficiency of nitrogen, and an excess number of vacancies exist in the polycrystals. This is the case for depositions between 525 and 575 °C. A peak position between 37.735 and 36.977 2θ degrees, which corresponds to a lattice parameter between 4.126 and 4.236 Å, suggests mixing of nitrogen, carbon and vacancies on the interstitial sublattice. This is the case for depositions at and above 600 °C. As mentioned above, however, β-WN_xC_y polycrystals may be forming even at the lower temperatures, with carbon playing a role in the lattice parameter increase at lower temperatures. While an explicit relationship between x and y in β-WN_xC_y cannot be determined from XRD and AES data, insight into the relation between carbon and vacancies on the interstitial sublattice is possible. Nitrogen prefers to occupy interstitial lattice sites in the polycrystals, and only resides at the grain boundary when its concentration in the film exceeds the β-W_2N stoichiometry. Low nitrogen levels in the **2b** films imply that all nitrogen resides at interstitial sites. Essentially constant, low nitrogen levels (Fig. 4) indicate that changes in lattice parameter will likely depend on the ratio of carbon to vacancies on the interstitial sublattice.

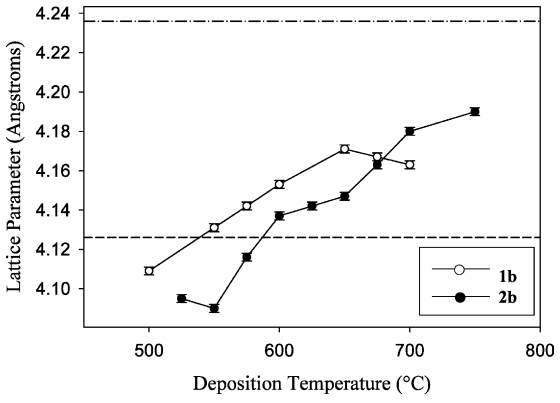

Fig. 5. Lattice parameters for films grown from **1b** and **2b**, based on the β-W_2N (111) diffraction peak. The dashed line at 4.126 Å represents the standard lattice parameter value for β-W_2N, while the dash–dot line at 4.236 Å is that for β-W_2C. Error bars indicate uncertainty in lattice parameter (±0.002 Å) due to X-ray Kα line broadening.

Values for lattice parameter in the films from **2b** tend to follow carbon content over the entire deposition temperature range. This likely reflects an increase in the ratio of carbon to vacancies on the interstitial sublattice with deposition temperature. The lattice parameter for the films from **2b** is 4.10 Å for 525 °C deposition, drops to 4.09 Å for 550 °C, and then increases to 4.14 Å for 600 °C. The carbon content follows the same trend (Fig. 4), decreasing from 525 to 550 °C, and then increasing up to 600 °C. The lattice parameter increases only slightly from a value of 4.14 Å at 600 °C to 4.15 Å at 650 °C, consistent with a small increase in carbon levels as measured by AES. This behavior is consistent with a decrease in compressive film stress, coupled with grain growth. Above 650 °C, the lattice parameter again increases with carbon content, reaching 4.19 Å at 750 °C.

3.6. Polycrystal grain size

Grain size (t) was estimated using the Scherrer equation (Eq. (1)) [47,48]. The two main causes of peak broadening in XRD thin film spectra are non-uniform film stress and the presence of small crystal grains. If we assume uniform film stress, the average crystallite size (t) may be estimated using the Scherrer equation:

$$t = \frac{0.9\lambda}{(B\cos\theta)} \quad (1)$$

where λ is the X-ray wavelength (1.5406 Å for Cu–K_α), B is the full width at half maximum (FWHM) for the selected diffraction peak and θ is the Bragg angle for that peak.

The dominant (111) diffraction peak for the films was used as the reference peak for FWHM determination. As depicted in Fig. 6, grain size for the films from **2b** increased with deposition temperature, varying from 35 to 67 Å over the 525–750 °C temperature range. Below 525 °C, the films were X-ray amorphous, hence, the

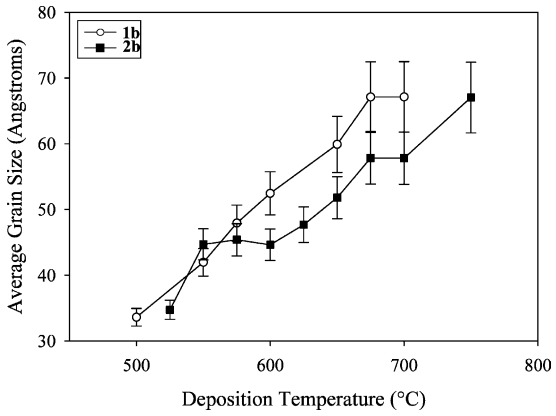

Fig. 6. Change in average grain size with deposition temperature for polycrystalline films grown from **1b** and **2b** based on the FWHM of the β-W_2N (111) diffraction peak. Error bars reflect uncertainty in FWHM measurements.

maximum grain size for amorphous films was below 35 Å. Interestingly, the grain size is essentially constant between 550 and 600 °C, which coincides with the transition region between kinetic and diffusion controlled growth. As the deposition temperature increases, a competition likely exists between increased grain growth due to higher surface diffusivity and decreased grain growth due to increasing carbon concentration on the film surface, which inhibits surface diffusion. Interplay between these phenomena causes grain growth in regions with small shifts in carbon content and leveling off of grain size in regions with larger shifts in carbon content.

3.7. Film growth rate

Growth rates were estimated by dividing the total film thickness (from X-SEM or AES sputter profile for the sample grown at 150 °C) by deposition time. Fig. 7 depicts X-SEM photos for films grown at the lowest and highest growth temperature, corresponding to deposition rates of 2 and 21 Å min^{-1}. An Arrhenius plot using the measured growth rates (Fig. 8) clearly delineates two growth regimes. The region with the shallow slope

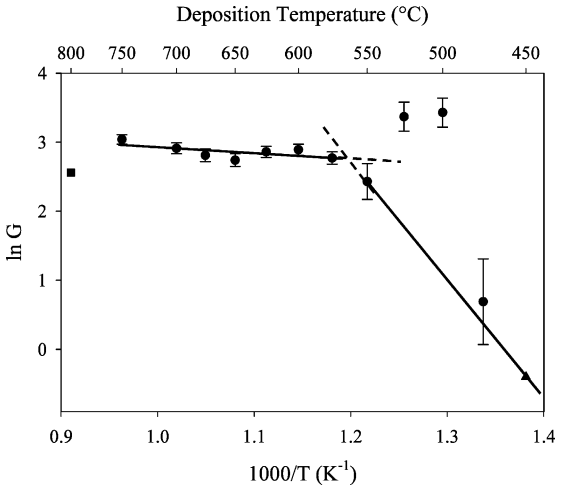

Fig. 8. Plot of WN_xC_y film growth rate (G, Å min^{-1}) from **2b** on Si(100) vs. inverse temperature. Error bars indicate uncertainty due to deposition temperature variation (±10 °C) and thickness measurement from X-SEM photos. The line fit for the kinetic regime includes data points for 450, 475 and 550 °C, and excludes points at 500 and 525 °C.

above 550 °C exhibits a weak dependence on temperature that is indicative of diffusion-controlled growth. The region with a steep slope below 550 °C suggests that growth is controlled by a kinetic process. In this regime, the rate-determining step for film growth is presumably reaction on the substrate surface. As observed in the XRD and AES studies (vide supra), the growth rates for films grown at 500 and 525 °C appear to be anomalous. This may be due to a decrease in the film density causing the measured thickness change to overestimate the reaction rate. Excluding the data points at 500 and 525 °C, a fit of the data gives an apparent activation energy for growth of films from **2b** in the kinetic regime as 1.41 ± 0.58 eV.

Depositions at 450 and 800 °C were done to establish the temperature boundaries for film growth from the phenylimido complex **2b**. Films deposited at 450 °C were not visible by X-SEM, but AES depth profiling indicated a nominal film thickness of ~100 Å. This

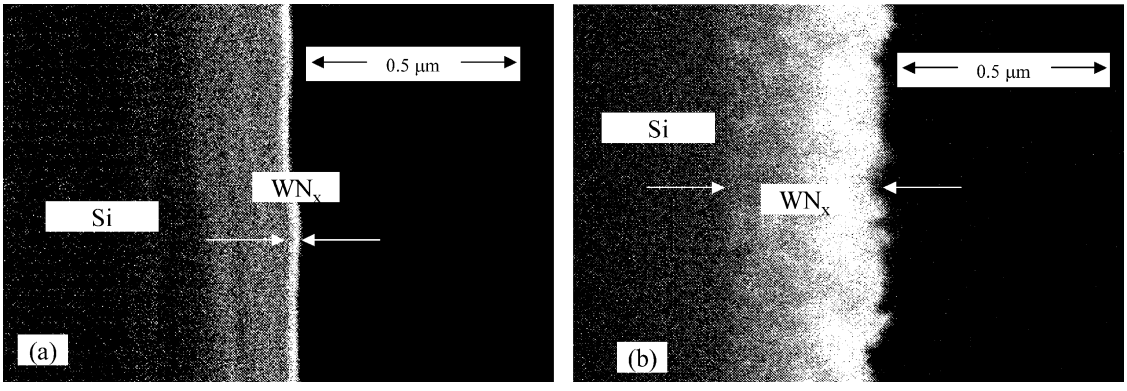

Fig. 7. Cross-sectional SEM photo depicting thickness of WN_xC_y film grown from **2b** on a Si (100) substrate grown at (a) 475 °C and (b) 750 °C.

thickness value (triangular symbol in Fig. 8) was used to estimate the value of the apparent activation energy for film growth in the kinetic regime. The growth rate at 800 °C dropped to 13 Å min^{-1} (square symbol in Fig. 8), with a high degree of surface roughness visible on the substrates after deposition. These results may be explained by either premature gas phase decomposition of the precursor, due to upstream heating at the higher temperature or by high desorption rate for a reactant species.

3.8. Film resistivity

Film resistivity was calculated as shown in Eq. (2), where ρ is resistivity (Ω-cm),

$$\rho = R_s t \quad (2)$$

R_s is sheet resistance as measured by 4-point probe (Ω/□), and t is film thickness determined by X-SEM (cm). The variation of film resistivity with deposition temperature is shown in Fig. 9. A deposition at 475 °C produced films with the lowest resistivity value (225 μΩ-cm) despite carbon and oxygen contamination levels of 3 and 15 at.%, respectively. This is lower than the 620 μΩ-cm reported for films grown from $(^tBuNH)_2W(N^tBu)_2$ at 650 °C [24,25], and also lower than the 750 μΩ-cm value observed for films grown from **1b**.

In the temperature range where anomalous growth was observed, 500–525 °C, the resistivity sharply increases, e.g. 73 000 μΩ-cm at 500 °C. This dramatic rise is consistent with deposition of tungsten oxide at 500 °C (vide supra). Interestingly, the resistivity climbs even higher to 87 000 μΩ-cm for deposition at 525 °C, despite XRD data consistent with polycrystalline β-WN_x. Moving to 550 °C, the film resistivity drops to 4750 μΩ-cm, then fluctuates somewhat with increasing growth temperature. Changes in the film resistivity above 550 °C occur due to the interplay of polycrystal grain growth, carbon content and film thickness. Increased grain growth generally causes a resistivity decrease, while increased carbon content and film thickness are associated with increased resistivity.

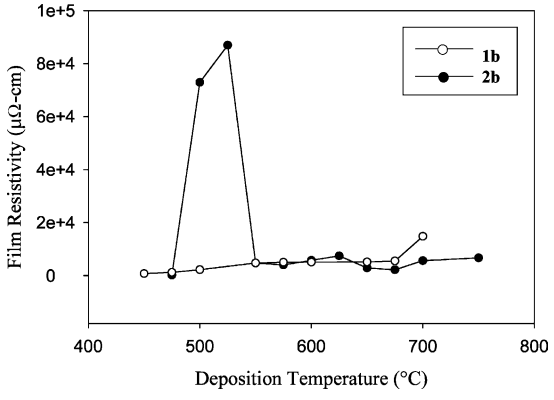

Fig. 9. Variation of film resistivity with deposition temperature for films deposited with **1b** and **2b**.

3.9. Film sheet resistance

Film resistivities calculated with Eq. (2) depend on both the sheet resistance and thickness of the analyzed films. As deposition temperature increases above 550 °C, the film thickness also increases. To decouple the impact of film thickness from the film's electrical properties, the sheet resistance was plotted as a function of deposition temperature (Fig. 10). The sheet resistance increases sharply with deposition temperature from 75 Ω/□ at 475 °C to 1600 Ω/□ at 500 °C, then rises further to 2000 Ω/□ at 525 °C. This increase in sheet resistance for the less conductive films grown at 500 and 525 °C indicates that these higher resistivity values (Fig. 9) are not due solely to higher film thickness and is consistent with oxide formation and the spike in carbon content (vide supra) determined by AES (Fig. 4). As the deposition temperature is increased to 550 °C, the sheet resistance decreases to 279 Ω/□, concomitant with lower oxygen and carbon content. The sheet resistance, like the resistivity, fluctuates somewhat for deposition temperature above 550 °C, but eventually reaches a constant value near 210 Ω/□ at 750 °C.

3.10. Comparison of films deposited from *1b* and *2b*

In terms of their decomposition chemistry, the most significant difference between isopropylimido complex **1b** and phenylimido complex **2b** is the dissociation energy of the N–C bond in the imido ligand. Based on data from organic model compounds, the N–C bond of isopropylimido complex **1b** is expected to be approximately 20 kcal mol^{-1} weaker than the analogous bond in **2b** [34]. Since cleavage of this bond is necessary for deposition of WN_x, one would expect there to be

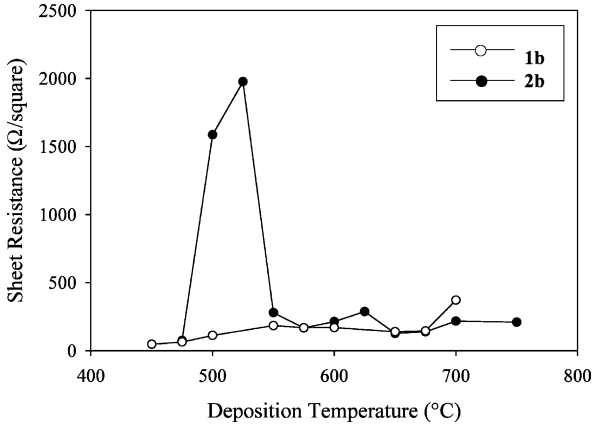

Fig. 10. Variation of film sheet resistance with deposition temperature for films deposited from **1b** and **2b**.

differences in film structure, film composition, and lattice parameter between films grown from the two precursors.

Amorphous film growth occurs below 500 °C for **1b** and **2b**. At 500 °C, a broad β-W_2N (111) polycrystalline peak appears for films from **1b**, while polycrystalline oxide peaks appear for the material from **2b**. Evidence of polycrystalline WN_x deposition from **2b** first appears at 525 °C. The anomalous film characteristics of material grown from **2b** at 500 °C appear to be linked to the presence of the Et_2O co-solvent (necessary because the solubilities of **1b** and **2b** differ). The maximum deposition temperature for films deposited from the isopropyl complex was 700 °C. Above this temperature, black particles were deposited on the substrate and susceptor, which subsequently compromised film quality. In contrast, deposition from phenylimido complex **2b** was possible up to 750 °C. The higher temperature limit for **2b** could be due to the enhanced N–C bond strength in its imido ligand.

Carbon levels in the films from **2b** were considerably lower than those from **1b** throughout the temperature range (Fig. 4). From 550 to 750 °C, films from both precursors exhibited a gradual rise in carbon content, with the isopropyl imido complex **1b** affording a steeper rise in carbon as growth temperature increased. Maximum nitrogen content for films from the two precursors occurred near their respective crystallization temperatures (500 °C for **1b** and 525 °C for **2b**). Throughout the temperature range studied, the nitrogen content in films deposited from **2b** was significantly lower than those grown from **1b**. The fact that films from phenylimido complex **2b** contained lower levels of both nitrogen and carbon than those from isopropylimido complex **1b** suggests that the phenylimido moiety is more likely to dissociate intact than the isopropylimido ligand. This is consistent with the higher N–C bond strength in the phenylimido group.

Corroborating evidence for this effect can be found in the mass spectra of **1a** and **2a**. Facile dissociation of the isopropyl group from **1a** is indicated by the observation of $[Cl_3WNH]^+$ at 78% abundance in the EI spectrum and detection of $[Cl_4WN]^-$ as the base peak in the NCI trace. Loss of the phenyl moiety from **2a** to yield the same ions does not occur under EI conditions and the NCI spectrum contains $[Cl_4WN]^-$ at only 4% abundance. Moderate amounts of $[Cl_4W]^+$ and $[Cl_3W]^+$ were detected in the mass spectra of **2b** under EI conditions, as well as fragments a–d (Fig. 1), which are consistent with what has previously been observed upon generation of NPh^+ from phenyl azide [33]. Although the mass spectral evidence for NPh loss consists of low intensity mass envelopes, their presence is significant. Because of the difference in conditions between mass spectrometry (ion chemistry) and MOCVD (thermal decomposition), the data in Fig. 1 and Table 1 do not rule out loss of NPh as a major heterogeneous process during deposition. Ideally, cleavage of the N–C bond in **2b** to release a phenyl group should occur during CVD of WN_x films. However, the high N–C dissociation energy would slow this process, allowing cleavage of the W–N bond to compete. Isopropylimido complex **1b**, with its weaker N–C bond, would be more likely to release the isopropyl moiety and leave the imido nitrogen in the growing film.

For both precursors, oxygen levels were highest for films deposited at the lower end of the temperature range (≤ 500 °C). AES indicated a decrease in oxygen content with increasing sputter depth into the films; hence, high oxygen levels were attributed to post-growth exposure of the films to air. The low density and high porosity of the amorphous structures grown at lower temperatures allow more rapid diffusion of oxygen from the air into the films and provide a large surface to volume ratio for adsorption. High oxygen levels in the films from **2b**, however, may be due to a combination of post-growth exposure to air and the presence of Et_2O during deposition. Increased carbon content in the films grown at higher temperatures is believed to inhibit post-growth oxygenation of the films by stuffing grain boundaries.

The lattice parameter shifts were also dependent on the precursor. Fig. 5 shows the lattice parameter increasing with temperature for films from both **1b** and **2b** at temperatures up to 650 °C, with films from **1b** having higher lattice parameter values throughout this range. This is expected, due to higher carbon content in films from the isopropylimido complex **1b**. Just above 675 °C, though, the lattice parameter in the films from **2b** becomes larger than that of the films from **1b**. Polycrystalline films deposited from **1b** have adequate nitrogen, even at high temperatures, to be considered primarily β-WN_x into which carbon is incorporated to form β-WN_xC_y. This β-WN_x, although nitrogen-deficient at higher temperatures, contains sufficient nitrogen to prevent a shift from formation of β-WN_xC_y toward β-WC_y, and leads to an upper limit in lattice parameter for films from **1b** near 4.16 Å. Thus, the decrease in lattice parameter in films from **1b** deposited above 650 °C was attributed to a solubility limit for carbon in β-WN_xC_y polycrystals with excess carbon residing at the grain boundaries above 675 °C.

The films from **2b**, however, contain so little nitrogen that tungsten is effectively left "bare" during deposition, enabling formation of carbide by reaction with depositing carbon at high temperature. Minimal nitrogen coupled with ~20 at.% carbon above 675 °C may mean that a shift away from deposition of β-WN_xC_y toward β-WC_y is occurring at high temperature with the **2b** precursor. The lattice parameter of 4.19 Å for films grown from **2b** at 750 °C indicates that the composition of the β-WN_xC_y polycrystals is nearing β-W_2C (i.e. x is

approaching zero and y is approaching 0.5), which has a lattice parameter of 4.236 Å.

Although β-WN_x films are reported to outperform β-WC_y for diffusion barrier applications, recent reports indicate interest in β-WN_xC_y as a potential barrier material. Thin films (~250 Å) of β-WN_xC_y have been deposited by atomic layer CVD onto various substrates (e.g. SiO_2, Cu, SiC and SiLK) by sequential reaction of WF_6, NH_3 and BEt_3 [49,50]. Addition of carbon to β-WN_x was reported to lower film resistivity. In addition, β-WN_xC_y with a composition ratio W:N:C ≈ 55:15:30 exhibited excellent adhesion to Cu. Hence, although films deposited from **2b** have low nitrogen content, this precursor may be of interest for β-WN_xC_y deposition. In addition, co-reactants could be used to raise the nitrogen content in material deposited from **2b**. We recently reported use of this strategy to dramatically increase the nitrogen content for films deposited from **1a**,**b** in the presence of NH_3 [51]. A similar approach may enable control of the nitrogen levels of β-WN_xC_y films from **2b**.

Nitrogen levels in the films from **2b** are much lower than films from **1b** at all temperatures. This trend in the films grown from the phenylimido precursor can again be attributed to the high N–C bond dissociation energy in the imido ligand of **2b**, which causes less nitrogen incorporation into the films, leaving open the possibility of β-WC_y formation. The XPS binding energy values for C1s and $W4f_{7/2}$ energy levels for films deposited from **2b** at 650 °C were 284.6 and 33.0 eV, respectively, while those for deposition at 750 °C, were 283.6 and 32.1 eV. These data are consistent with a shift toward formation of the β-WC_y phase for the film deposited from **2b** at 750 °C [52]. The XPS results for films from **1b** did not indicate this shift. This suggests that adequate nitrogen remained in the polycrystals to prevent a shift to carbide formation, forcing additional carbon to deposit at the grain boundaries.

Grain growth behavior was similar for the two precursors. Grain sizes for films grown from **1b** and **2b** increased from lowest to highest deposition temperature, with those from **2b** generally having smaller size grains than those from **1b**. Above 600 °C, where both precursors are operating in the diffusion controlled regime, the films from **2b** required a temperature increase of ~50 °C to deposit grains of similar size to their **1b** counterparts. This observation can again be traced to the difference in the strengths of imido N–C bonds in the precursors, with the weaker isopropyl imido bond affording higher growth rate and grain size for a given deposition temperature.

Deposition rates from the phenylimido complex **2b** films were lower than those from the isopropylimido complex **1b**. Film deposition rates ranged from 10 to 27 Å min^{-1} for films from **1b**, while the range was 2–21 Å min^{-1} for films from **2b**. The calculated E_a for film growth from **2b** in the kinetically controlled regime was 1.41 ± 0.58 eV, as compared to 0.84 eV for **1b** and 0.9 eV for $(^tBuNH)_2W(N^tBu)_2$ [24,25]. The higher activation energy for **2b** is consistent with cleavage of the stronger imido N–C bond before or during the rate-determining step of the deposition process. Interestingly, the E_a for **2b** is above the typical activation energy range for CVD growth in the kinetic regime, which is 0.5 to 1 eV [53].

With the exception of the anomalous results for growth at 500 and 525 °C, comparison of the sheet resistances, which negate the impact of film thickness on electrical properties, shows that the films from **1b** and **2b** have similar electrical properties when deposited at or below 675 °C. Above 675 °C, **1b** films have higher sheet resistance than **2b** films, consistent with the high carbon levels in the **1b** films, which scatter electrons flowing through the material.

3.11. Conclusions

The tungsten imido complex $Cl_4(CH_3CN)W(NPh)$ **2b** was tested to determine its suitability as a single-source precursor for low temperature growth of β-WN_x thin films. Comparison of the film growth properties of **2b** to those of its isopropylimido analogue **1b** allows evaluation of the effect of the imido N–C bond dissociation energy on film growth and properties. Films deposited from **2b** were deficient in nitrogen compared to those from **1b**, consistent with a tendency of the stronger imido N–C bond of **2b** to result in dissociation of intact NPh fragments during deposition. Since its films contain more nitrogen and have lower amorphous deposition temperatures and sheet resistances, the isopropyl imido precursor **1b** is superior to **2b** for β-WN_x barrier deposition.

Acknowledgements

The authors would like to thank the staff of the Major Analytical Instrumentation Center (MAIC) at the University of Florida for assistance with film characterization. Special thanks go to Eric Lambers for assistance with AES and to Wayne Acree for assistance with X-SEM. The Office of Naval Research provided support under grant numbers N00014-95-1-0563 and N00014-99-1-0841. Funding for the residual gas analyzer was provided by the Air Force Office of Scientific Research.

References

[1] E. Kolawa, P.J. Pokela, J.S. Reid, J.S. Chen, M.A. Nicolet, Appl. Surf. Sci. 53 (1991) 373.
[2] J. Baumann, C. Kaufmann, M. Rennau, T. Werner, T. Gessner, Microelectronic Eng. 33 (1997) 283.

[3] M.A. Nicolet, Thin Solid Films 52 (1978) 415.
[4] M.A. Nicolet, M. Bartur, J. Vac. Sci. Technol. 19 (1981) 786.
[5] B.M. Ekstrom, S. Lee, N. Magtoto, J.A. Kelber, Appl. Surf. Sci. 171 (2001) 275.
[6] N. Shamir, J.C. Lin, R. Gomer, Surf. Sci. 214 (1989) 74.
[7] C.H. Winter, Aldrichim. Acta 33 (2000) 3.
[8] A.R. Ivanova, C.J. Galewski, C.A. Sans, T.E. Seidel, S. Grunow, K. Kumar, A.E. Kaloyeros, Mater. Res. Soc. Symp. Proc. 564 (1999) 321.
[9] C. Galewski, T. Seidel, Eur. Semiconductor (1999) 31.
[10] M.J. Shaw, S. Grunow, D.J. Duquette, J. Electron. Mater. 30 (2001) 1602.
[11] S.D. Marcus, R.F. Foster, Thin Solid Films 236 (1993) 330.
[12] M. Nagai, K. Kishida, Appl. Surf. Sci. 70–1 (1993) 759.
[13] C.W. Lee, Y.T. Kim, C. Lee, J.Y. Lee, S.K. Min, Y.W. Park, J. Vac. Sci. Technol. B 12 (1994) 69.
[14] T. Nakajima, K. Watanabe, N. Watanabe, J. Electrochem. Soc. 134 (1987) 3175.
[15] M. Nagai, K. Kishida, S. Omi, Nippon Kagaku Kaishi (1996) 368.
[16] M. Nagai, K. Kishida, S. Omi, Nippon Kagaku Kaishi (1994) 907.
[17] K. Iguchi, M. Urai, C. Shiga, M. Koba, JP Patent 01005015, 1989.
[18] L. Volpe, M. Boudart, J. Solid State Chem. 59 (1985) 332.
[19] S. Ganguli, L. Chen, T. Levine, B. Zheng, M. Chang, J. Vac. Sci. Technol. B 18 (2000) 237.
[20] Y.T. Kim, S.K. Min, Appl. Phys. Lett. 59 (1991) 929.
[21] A.L. Currie, K.E. Howard, J. Mater. Sci. 27 (1992) 2739.
[22] J.E. Kelsey, C. Goldberg, G. Nuesca, G. Peterson, A.E. Kaloyeros, B. Arkles, J. Vac. Sci. Technol. B 17 (1999) 1101.
[23] R.G. Gordon, S. Barry, R.N.R. Broomhall-Dillard, V.A. Wagner, Y. Wang, Mater. Res. Soc. Symp. Proc. 612 (2000) D9.12/1.
[24] H.T. Chiu, S.H. Chuang, J. Mater. Res. 8 (1993) 1353.
[25] M.H. Tsai, S.C. Sun, H.T. Chiu, S.H. Chuang, Appl. Phys. Lett. 68 (1996) 1412.
[26] E.L. Crane, H.-T. Chiu, R.G. Nuzzo, J. Phys. Chem. B 105 (2001) 3549.
[27] S.W. Johnston, C.G. Ortiz, O.J. Bchir, Y. Zhang, L. McElwee-White, T.J. Anderson, M.D. Allendorf, T.M. Besmann (Eds.), Chemical Vapor Deposition: CVD XV (15th), Vol. 2000-13, Electrochemical Society, Pennington, NJ, 2000. 268–276.
[28] O.J. Bchir, S.W. Johnston, A.C. Cuadra, T.J. Anderson, C.G. Ortiz, B.C. Brooks, D.H. Powell, L. McElwee-White, J. Cryst. Growth 249 (2003) 262.
[29] S.F. Pederson, R.R. Schrock, J. Am. Chem. Soc. 104 (1982) 7483.
[30] A.J. Nielson, J.M. Waters, Aust. J. Chem. 36 (1983) 243.
[31] T.S. Lewkebandara, P.H. Sheridan, M.J. Heeg, A.L. Rheingold, C.H. Winter, Inorg. Chem. 33 (1994) 5879.
[32] L.V. Interrante, G.A. Sigel, M. Garbauskas, C. Hejna, G.A. Slack, Inorg. Chem. 28 (1989) 252.
[33] W.D. Crow, C. Wentrup, Tetrahedron Lett. (1967) 4379.
[34] S.W. Benson, Thermochemical Kinetics, 2nd ed, Wiley-Interscience, New York, 1976, p. 309.
[35] C.J.M. Fletcher, G.K. Rollefson, J. Am. Chem. Soc. 58 (1936) 2129.
[36] J.F. Foucaut, R. Martin, Int. J. Chem. Kinetics 11 (1979) 789.
[37] S. Ingrey, M.B. Johnson, R.W. Streater, G.I. Sproule, J. Vac. Sci. Technol. 20 (1982) 968.
[38] K.C. Park, K.B. Kim, I. Raaijmakers, K. Ngan, J. Appl. Phys. 80 (1996) 5674.
[39] S.J. Wang, H.Y. Tsai, S.C. Sun, J. Electrochem. Soc. 148 (2001) C563.
[40] M. Eizenberg, K. Littau, S. Ghanayem, A. Mak, Y. Maeda, M. Chang, A.K. Sinha, Appl. Phys. Lett. 65 (1994) 2416.
[41] D.R. Lide, JANAF Thermochemical Tables, 3rd ed, American Institute of Physics, New York, 1985.
[42] Y.M. Lakhtin, Y.D. Kogan, T.M. Borovskaya, G.A. Solodkin, Russ. Metall. (1979) 158.
[43] P. Gustafson, Mater. Sci. Technol. 2 (1986) 653.
[44] P.J. Pokela, C.K. Kwok, E. Kolawa, S. Raud, M.A. Nicolet, Appl. Surf. Sci 53 (1991) 364.
[45] S.H. Kim, D.S. Chung, K.C. Park, K.B. Kim, S.H. Min, J. Electrochem. Soc. 146 (1999) 1455.
[46] K.M. Chang, I.C. Deng, T.H. Yeh, K.D. Lain, C.M. Fu, Jpn. J. Appl. Phys. Part 1-Regul. Pap. Short Notes Rev. Pap. 38 (1999) 1343.
[47] B.D. Cullity, Elements of X-Ray Diffraction, Addison-Wesley, Reading, MA, 1978.
[48] M. Nagai, N. Hirano, S. Omi, Jpn. J. Appl. Phys. Part 1-Regul. Pap. Short Notes Rev. Pap. 39 (2000) 4558.
[49] W.-M. Li, K. Elers, J. Kostamo, S. Kaipio, H. Huotari, M. Soininen, P.J. Soininen, M. Tuominen, S. Haukka, S. Smith, W. Besling, In: Proceedings of the IEEE International Interconnect Technology Conference, 5th, Burlingame, CA, USA, June 3–5, 2002, 2002, pp. 191–193.
[50] S. Smith, W.-M. Li, K.-E. Elers, K. Pfeifer, Microelec. Eng. 64 (2002) 247.
[51] O.J. Bchir, T.J. Anderson, B.C. Brooks, L. McElwee-White, In: Chemical Vapor Deposition: CVD XVI (16th); M. Allendorf, F. Maury, F. Teyssandier (Eds.), Electrochemical Society: Pennington, NJ, 2003; Vol. 2003–08, pp 424–431.
[52] S.H. Koutzaki, J.E. Krzanowski, J.J. Nainaparampil, Metall. Mater. Trans. A-Phys. Metall. Mater. Sci. 33 (2002) 1579.
[53] I.J. Raaijmakers, J. Yang, Appl. Surf. Sci. 73 (1993) 31.